



# Nitrogen-doped reduced graphene oxide supports for noble metal catalysts with greatly enhanced activity and stability

Daping He, Yulin Jiang, Haifeng Lv, Mu Pan, Shichun Mu\*

State Key Laboratory of Advanced Technology for Materials Synthesis and Processing, Wuhan University of Technology, Wuhan 430070, China

## ARTICLE INFO

### Article history:

Received 20 July 2012

Received in revised form

27 November 2012

Accepted 6 December 2012

Available online 16 December 2012

### Keywords:

Catalysts

Reduced graphene oxide

Nitrogen-doping

Oxygen reduction reaction

Proton exchange membrane fuel cells

## ABSTRACT

Pt nanoparticles supported on nitrogen-doped reduced graphene oxide (NRGO) were investigated for use as proton exchange membrane fuel cell catalysts. Artfully, NRGO was synthesized using a lyophilisation-assisted N-doping method, and simultaneous reduction of graphene oxide (GO) was achieved. A nitrogen content as high as 5.06% was obtained with pyridinic-N as the dominant nitrogen species. Pt nanoparticles with an average diameter of 2.5 nm were uniformly loaded on NRGO using impregnation methods. Both cyclic voltammetry and oxygen reduction reaction (ORR) measurements revealed a higher catalytic activity and lower losses of the electrochemically active surface area of this novel Pt/NRGO catalyst in comparison to those of the Pt/GO and conventional Pt/C catalysts. Significantly, the catalytic activity of the Pt/NRGO in ORR showed almost no degradation even after 1000 potential cycles, indicating that our new catalysts have excellent stability. A mechanism for improving the ORR activity and the stability of the Pt/NRGO was tentatively proposed and discussed.

© 2012 Elsevier B.V. All rights reserved.

## 1. Introduction

Nanostructured carbon materials, such as carbon nanotubes (CNTs), carbon nanofibers, and recently discovered graphene nanosheets (GNS), have been studied extensively as catalyst supports for proton exchange membrane (PEM) fuel cells due to their specific electronic and micro- and macro-structural characteristics [1–4]. GNS exhibit a unique structure of two-dimensional sheets that are one atom thick and composed of  $sp^2$ -bonded carbon atoms. They possess stable physical properties, large surface areas (theoretical specific surface area of  $2600\text{ m}^2\text{ g}^{-1}$ ) and high electrical conductivities [5–7]. Significantly, GNS provide an opportunity for employing two-dimensional materials as the conductive sheets to anchor electrocatalysts in PEM fuel cells. Unfortunately, the efficient attachment of Pt nanoparticles (NPs) to GNS with a uniform distribution remains a big challenge because of the inert graphitized surface nature of GNS.

Many efforts have been made to further modulate the properties of GNS over the past several years [8–10]. In particular, the doping of nitrogen (N) into carbon structures has received great attention [11–14]. Many previous researchers have reported that N-doped carbon nanostructures with n-type or metallic behaviour are expected to have greater electron mobility than their corresponding undoped carbon nanostructures. Moreover, N-doping

efficiently introduces chemically active sites for use in catalytic reactions and anchoring sites for metal nanoparticle deposition [9,10,15–17]. Several routes have been employed for the synthesis of N-doped GNS, including joule annealing in  $\text{NH}_3$ , nitrogen plasma, chemical vapour deposition, arc discharge of carbon electrodes and hydrothermal reduction in the presence of N-containing precursors [15–20]. However, the most established N sources used for N-graphene, including  $\text{NH}_3$  and ammonia, are harshly corrosive and have the potential to damage the intrinsic properties of and Pt active sites on GNS [21–23].

Recently, it was found that urea, with its high N content (46 wt%), can be used as a mild N-containing precursor for the nitridation of various materials at a moderate temperature [24–26]. In this study, we report a simple and mild approach for the production of N-doped graphene by introducing urea as an N-containing precursor and using lyophilisation (freeze-drying). In our previous work, it was found that lyophilisation readily assists in the uniform dispersion of CNTs and effectively prevents metal particles from agglomerating [27]. Herein, we show that a well-mixed solution of graphene oxide (GO) and urea in deionized water can be completely dried by lyophilisation without restacking of the GO sheets during the drying process. Additionally, a high nitrogen content and a tunable reduction of GO are expected to be achieved simultaneously by subsequent thermal treatment in an inert gas. Moreover, N-doping is accompanied by the reduction of GO, which restores the hybridized  $sp^2$  graphite network and contributes to the conductivity and stability of GO. Recently, Wei et al. have reported that the electrical conductivity of thermally reduced GO (RGO) is up to four

\* Corresponding author. Tel.: +86 27 87651837; fax: +86 27 87879468.

E-mail addresses: [mshc@whut.edu.cn](mailto:mshc@whut.edu.cn), [mushichun@gmail.com](mailto:mushichun@gmail.com) (S. Mu).

orders of magnitude greater than that of pristine GO [28]. Significantly, we believe that a greatly enhanced activity and stability can be achieved by using this N-doped RGO (NRGO) as a Pt catalyst support for PEM fuel cell applications.

## 2. Experimental

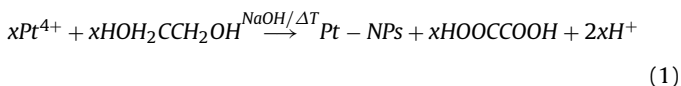
### 2.1. Preparation of catalysts

GO was synthesized from natural graphite flakes using a modified Hummers method [29]. Graphite powder (2.0 g) was pre-oxidised in a concentrated  $\text{H}_2\text{SO}_4$  solution (150 mL), into which  $\text{NaNO}_3$  (2 g) had been added and completely dissolved.  $\text{KMnO}_4$  (15 g) was slowly added to the mixture under vigorous agitation, and the reaction flask was subsequently heated to  $40^\circ\text{C}$ . The reaction was carried out for 40 h, during which the mixture became pasty and underwent a colour change gradually from dark green to reddish brown. The slurry was diluted with 250 mL of deionized water to terminate the reaction. The colour of the mixture immediately turned to bright yellow following treatment with 10 mL of 30 wt%  $\text{H}_2\text{O}_2$  to reduce the insoluble manganese species to  $\text{Mn}^{2+}$  ions. The suspension stood overnight to allow the precipitate to settle out and then was centrifuged to decant the supernatant. After the precipitate was repeatedly rinsed with deionized water to remove metal ions, the formation of a viscous brown dispersion was eventually observed. Then, the graphite oxide dispersion was concentrated and lyophilised to yield fluffy powders. Finally, homogeneous and stable GO colloids were obtained by ultrasonic exfoliation of a diluted graphite oxide hydrogel with a known concentration. The mixture was bath-sonicated for 10 min and then centrifuged for 5 min. The supernatant, which contained almost exclusively single sheets of GO, was collected.

As illustrated in Scheme 1, GO and urea were mixed in a mass ratio of 1:10 and dispersed in deionized water. The mixture was thoroughly dispersed by ultrasonication for 30 min, and most of the water was subsequently removed under reduced pressure in a rotary evaporator. The resultant mixture was completely dried by lyophilisation, and then the solid phase was put in a quartz boat in the centre of a tube furnace. After flowing Ar for approximately 20 min, the furnace was heated to  $600^\circ\text{C}$  in 30 min and subsequently cooled to room temperature under flowing Ar. The

samples were removed from the tube reactor after the furnace temperature was below  $30^\circ\text{C}$ . The resulting N-doped NRGO was achieved by splitting the graphite oxide into the reduced GO sheets through the evolution of  $\text{CO}_2$ .

The Pt NPs on NRGO were synthesized in an alkaline ethylene glycol solution. The alcohol groups on ethylene glycol are easily oxidized to aldehyde groups, which are unstable in solution and further oxidized to acid groups. In this reaction pathway, Pt ions interact with the functional groups, which reduce the Pt ions to Pt NPs [30]. The overall reaction is

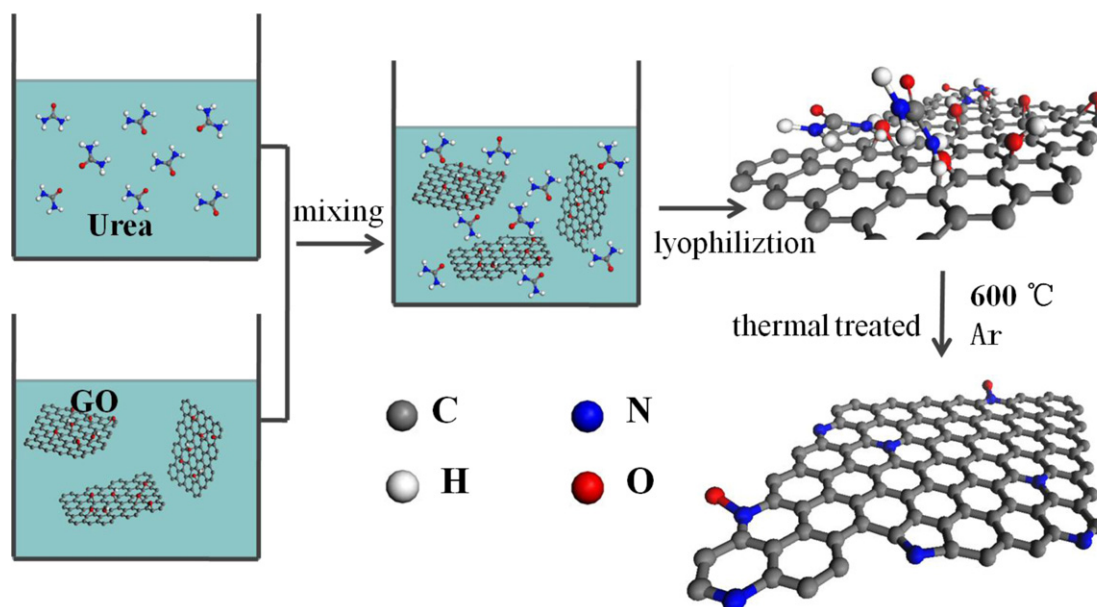


Twenty millilitres of  $\text{H}_2\text{PtCl}_6 \cdot \text{H}_2\text{O}$  ( $1.5 \text{ mg mL}^{-1}$ ) and 100 mL of ethylene glycol were mixed and vigorously stirred for 20 min at  $25^\circ\text{C}$ , and then the pH of the solution was adjusted to 8–10 using a 1 M NaOH solution. The colloidal Pt NPs were obtained after refluxing at  $130^\circ\text{C}$  for 1–2 h until the solution colour changed from yellowish to black. Then, one hundred milligrams of NRGO previously suspended in 50 mL of ethylene glycol by ultrasonic stirring for 30 min were added to the Pt colloid, and the mixture was agitated for 11 h. After filtration, washing with deionized water, and drying at  $100^\circ\text{C}$  in a vacuum oven, a Pt/NRGO catalyst with 20 wt% Pt loading was prepared. As a benchmark, the Pt/GO catalyst was prepared using the same method. Commercial Pt/C catalyst (20% Pt supported on Vulcan XC-72 carbon) was purchased from JM.

### 2.2. Characterisation of catalysts

Crystalline phases presented in these samples were determined from the XRD patterns. Diffractograms were recorded on a Polycrystal PANalytical X'Pert Pro apparatus using Ni-filtered  $\text{Cu K}\alpha$  radiation and a graphite monochromator. XRD scans were performed at a rate of  $2^\circ \text{ min}^{-1}$  from  $20$  to  $90^\circ$ . The average crystalline size of the Pt NPs can be obtained according to the Scherrer equation [31]:

$$D = \frac{k\lambda}{\beta \cos \theta} \quad (2)$$



Scheme 1. Schematic of the synthetic procedures of the NRGO.

where  $k=0.89$ ,  $\lambda$  (the X-ray wave length for Cu radiation) = 0.1541 nm,  $\beta$  is the half-height peak width,  $\theta$  is the Bragg angle corresponding to the peak maximum, and  $D$  denotes the average diameter of the crystal pellets.

Morphologies of the prepared catalysts were analysed with a JEOL 2010 high-resolution transmission electron microscope (HRTEM). The prepared catalysts were dispersed ultrasonically in ethanol, and then an aliquot of this solution was deposited onto a lacey-carbon/Cu grid (200 mesh) and dried at room temperature before TEM analysis. XPS measurements were performed with a VG Scientific ESCALAB 210 electron spectrometer using Mg K $\alpha$  radiation ( $h\nu = 1253.6$  eV, 300 W) under a vacuum of  $2 \times 10^{-8}$  Pa. The binding energy was referenced to the C 1s line at 284.6 eV. The error in the determination of electron binding energies and line widths did not exceed 0.2 eV. Raman spectra were measured using an excitation wavelength of 457.9 nm provided by a Spectra-Physics Model 2025 argon ion laser. The laser beam was focused to a 0.10-mm diameter spot on the sample with a laser power of 1 mW. The samples were pressed into a depression at the end of a 3-mm diameter stainless steel rod, which was held at a 30° angle in the path of the laser beam.

The electrochemical measurements were performed using an Autolab PGSTAT 30 potentiostat (Eco Chemie BV, Holland) with a three-electrode setup. A saturated calomel electrode (SCE) was used as the reference electrode, and platinum wire was used as a counter electrode. For convenience, all potentials are hereafter referred to a reversible hydrogen electrode (RHE). Six milligrams of catalyst powders were mixed with 1000  $\mu$ L of deionized water and 42  $\mu$ L of a 5 wt% Nafion solution and coated on a mirror-polished glassy carbon disk electrode ( $d = 5.0$  mm) as a working electrode. The measurements were carried out in 0.5 M H<sub>2</sub>SO<sub>4</sub> at a scan rate of 50 mV s<sup>-1</sup> over a potential range of 0 to 1.2 V vs. RHE at room temperature. The H<sub>2</sub>SO<sub>4</sub> solution was saturated with pure argon to expel oxygen from the solution. The specific electrochemical active area (ECA) was calculated from the following equation [32,33]:

$$ECA = \frac{Q_H}{m \times q_H} \quad (3)$$

where  $Q_H$  is the charge for H<sub>upd</sub> ( $H^+ + e^- = H_{upd}$ ) adsorption,  $m$  is the metal loading, and  $q_H$  (210  $\mu$ C cm<sup>-2</sup>) is the charge required for monolayer adsorption of hydrogen on Pt surfaces.

Electrochemical impedance spectroscopy (EIS) was measured by a EC-lab SP300 frequency response analyzer and the frequency ranged from 1 MHz to 1 Hz. Electrochemical accelerated durability tests (ADT) were employed to evaluate the long-term performance of the catalysts. ADT is an inexpensive and time-effective method for screening catalysts for high stability and good performance [34]. Using the same system as in a CV test, ADT was conducted in the current study with CV curves between 0.6 and 1.20 V. The ORR performance of the as-prepared catalysts was evaluated by the rotating disk electrode (RDE) technique in a 0.5 M H<sub>2</sub>SO<sub>4</sub> electrolyte at a sweep rate of 10 mV s<sup>-1</sup> and a speed of 1600 rpm at room temperature.

### 3. Results and discussion

Fig. 1A displays the Raman spectra of the as-made GO and NRGO. Both of the samples have D bands, which correspond to sp<sup>3</sup>-hybridized carbons and signify the presence of disordered graphite, and G bands from sp<sup>2</sup>-hybridized carbons indicative of the ordered state in the curved GNS [35,36]. The intensity of the D band is higher than that of the G band in GO, revealing the presence of many defects and oxygen functional groups in the as-prepared GO. By contrast, NRGO shows a lower D to G ratio compared to GO, suggesting an increase in the size of C sp<sup>2</sup> atom clusters as a result of the simultaneous reduction of GO. It is noteworthy that the G

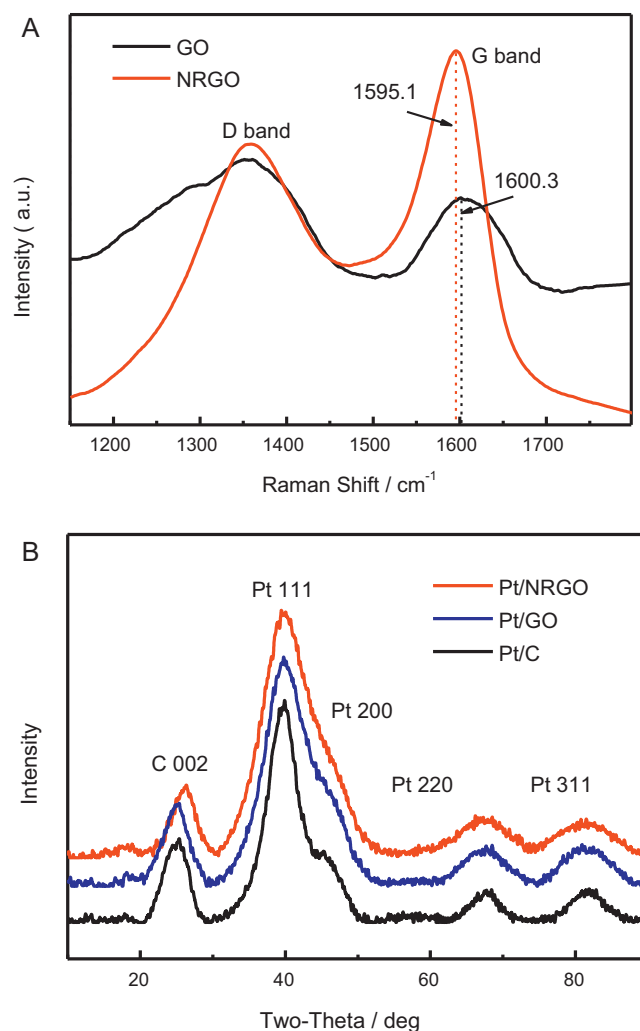


Fig. 1. Raman spectra of GO and NRGO (a), XRD patterns of the Pt/NRGO, Pt/GO and Pt/C catalysts (b).

band shifts with nitrogen doping; the G peak positions of the as-prepared GO and NRGO are approximately 1600.3 and 1595.1 cm<sup>-1</sup>, respectively. If we assume all other factors (e.g., defects, layer numbers, strains) in the GO samples are the same, the redshift of the G

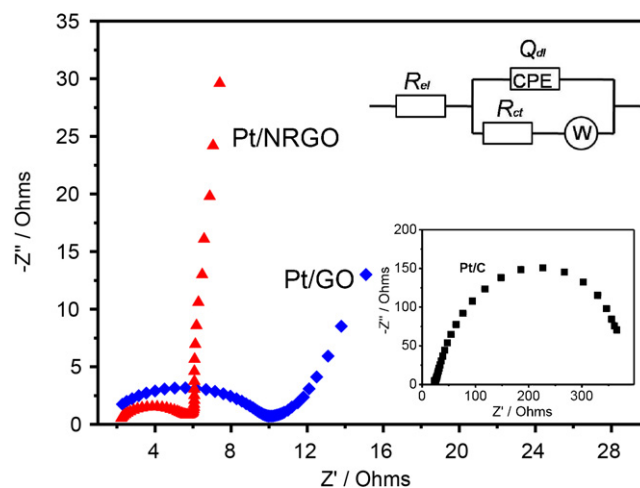


Fig. 2. Nyquist plots of EIS for Pt/NRGO, Pt/GO and Pt/C (figure inset, bottom) in 0.5 M H<sub>2</sub>SO<sub>4</sub>. The inset (top) is the equivalent circuit used to fit the impedance spectra.



peak could be due to N-doping, which is consistent with what has been observed in similarly N-doped graphene [37,38].

The XRD patterns of the Pt/NRGO, Pt/GO and Pt/C catalysts are shown in Fig. 1B. The peaks between 30 and 90° can be indexed to Pt crystals with a face-centred cubic (fcc) structure. The peaks at  $2\theta = 39.7, 46.5, 67.7$ , and  $81.4^\circ$  are assigned to the (1 1 1), (2 0 0), (2 2 0), and (3 1 1) planes of Pt, respectively. The volume-averaged particle size was calculated according to the Scherrer equation. From the full-width half-maximum of the (2 2 0) peak, the average Pt particle sizes are 2.5, 2.8, and 3.2 nm for Pt/NRGO, Pt/GO, and Pt/C, respectively.

Fig. 2 presents the Nyquist plots of EIS for the Pt/NRGO, Pt/GO and Pt/C obtained in 0.5 M  $\text{H}_2\text{SO}_4$  at open potential. The EIS plots of all samples contain a partially overlapped semicircle. The charge transfer resistance in different catalysts can be estimated from

the analysis of EIS spectra by using the software ZsimpWin based on an equivalent electric circuit as shown in the inset of Fig. 2, where the  $R_{el}$  represents the uncompensated solution resistance,  $R_{ct}$  is charge transfer resistance of the catalyst and  $Q_{dl}$  is a constant phase element [39–41]. The sequence of the values of  $R_{ct}$  for different electrodes is Pt/C ( $413.4 \Omega$ ) > Pt/GO ( $7.5 \Omega$ ) > Pt/NRGO ( $3.14 \Omega$ ). Obviously, the  $R_{ct}$  values in graphene based composites are much lower than that of the Pt/C, implying graphene is a more appropriate electrocatalyst support for PEM fuel cells. In addition, the Pt/NRGO shows a remarkably lower  $R_{ct}$  value ( $3.14 \Omega$ ) than that of Pt/GO ( $7.5 \Omega$ ), which can be contributed to the N-doping accompanied by the reduction of GO.

Fig. 3 displays representative TEM images of the Pt NPs distribution of the Pt/NRGO, Pt/GO and conventional Pt/C catalysts. The TEM images (Fig. 3A) show the presence of uniform, well-dispersed Pt

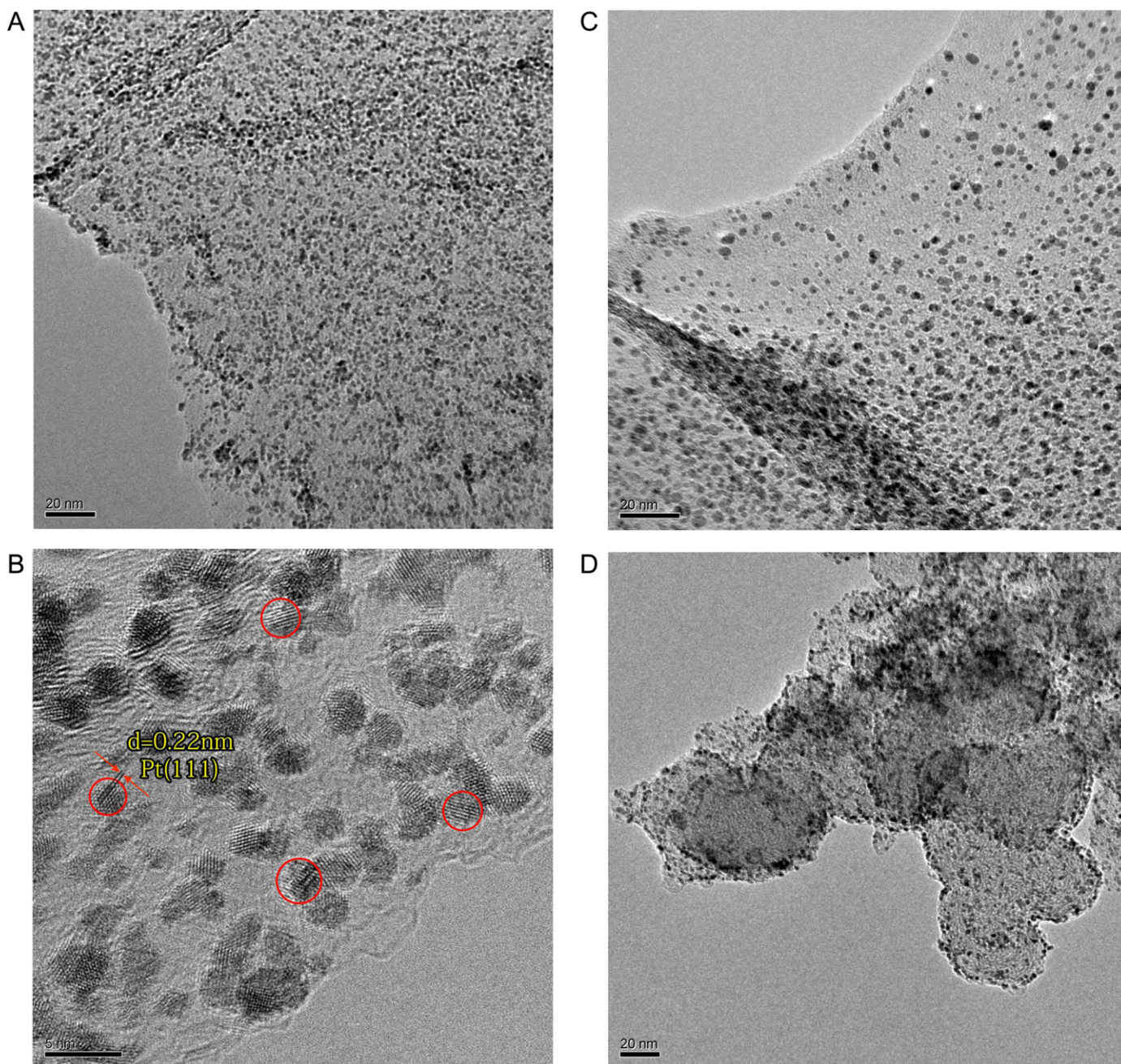


Fig. 3. Transmission electron microscope (TEM) images of the Pt/NRGO (a, b), Pt/GO (c) and Pt/C catalysts (d).

**Table 1**

Particle size distribution of Pt/NRGO, Pt/GO and Pt/C before and after 4000 cycles.

Samples	Particle size distribution (nm)	Mean size (nm)
Pt/NRGO	1–4	2.5
After 4000 cycles	2–10	4.5
Pt/GO	1–6	2.8
After 4000 cycles	4–14	8.9
Pt/C	2–6	3.2
After 4000 cycles	5–20	10.6

NPs on NRGO over very large areas of several microns, and these NPs exhibit no aggregation into larger clusters and form an adlayer-like pattern with uniform particle sizes. A high-resolution TEM image for the Pt/NRGO clearly shows that the distance between two adjacent lattice planes of the Pt NPs is approximately 0.22 nm, which indicates a crystalline Pt structure (Fig. 3B). Table 1 displays the particle size distribution calculated from approximately 200 particles (as shown in Figure S1). For the Pt/NRGO catalyst, a very narrow particle size distribution of the Pt NPs is found with sizes mostly falling between 1.0 and 4.0 nm (mean size 2.5 nm). However, the Pt NPs supported on GO have a larger mean size (2.8 nm) with a broader particle size distribution from 1.0 to 6.0 nm (Fig. 3C). The statistical survey results suggest a lower agglomeration of the Pt NPs on NRGO than of those on GO. It is evident that the introduction of nitrogen into the carbon structure is responsible for the Pt deposition. The Pt particle size of the conventionally available Pt/C

**Table 2**

Elemental analysis of GO and NRGO.

Samples	C (wt%)	N (wt%)	O (wt%)
GO	61.3.	–	38.7
NRGO	86.01.	5.06	8.93

catalyst, which is used as a reference, is comparable to that of the Pt/GO catalyst (Fig. 3D). It should be noted that few defects were created in NRGO with the mild lyophilisation-assisted N-doping method.

Fig. 4A shows the XPS spectra of the Pt/NRGO, Pt/GO and Pt/C catalysts. In addition to the C 1s and O 1s signals at 284.6 and 543.1 eV, respectively, the Pt 4f, Pt 5s, Pt 4p and Pt 4d signals appear in both samples [42]. It should be noted that the occurrence of the N 1s signal in NRGO confirms the incorporation of N into graphene. Table 2 lists the elemental analysis of GO and NRGO obtained from the XPS results. After the N-doping process, the N content of NRGO is 5.06 wt%, while the oxygen content decreases to 8.93 wt%. The results verify that the oxygen-containing functional groups could be removed during the N-doping process. The XPS spectra were fit to obtain detailed information about the chemical bonding energy (BE) of the nitrogen (Fig. 4B). There are at least four nitrogen functional groups in N-doped carbon in this work, including pyridinic-N (N1, BE =  $398.6 \pm 0.3$  eV), pyrrolic-N (N2, BE =  $400.3 \pm 0.4$  eV), quaternary-N (N3, BE =  $401.3 \pm 0.3$  eV),

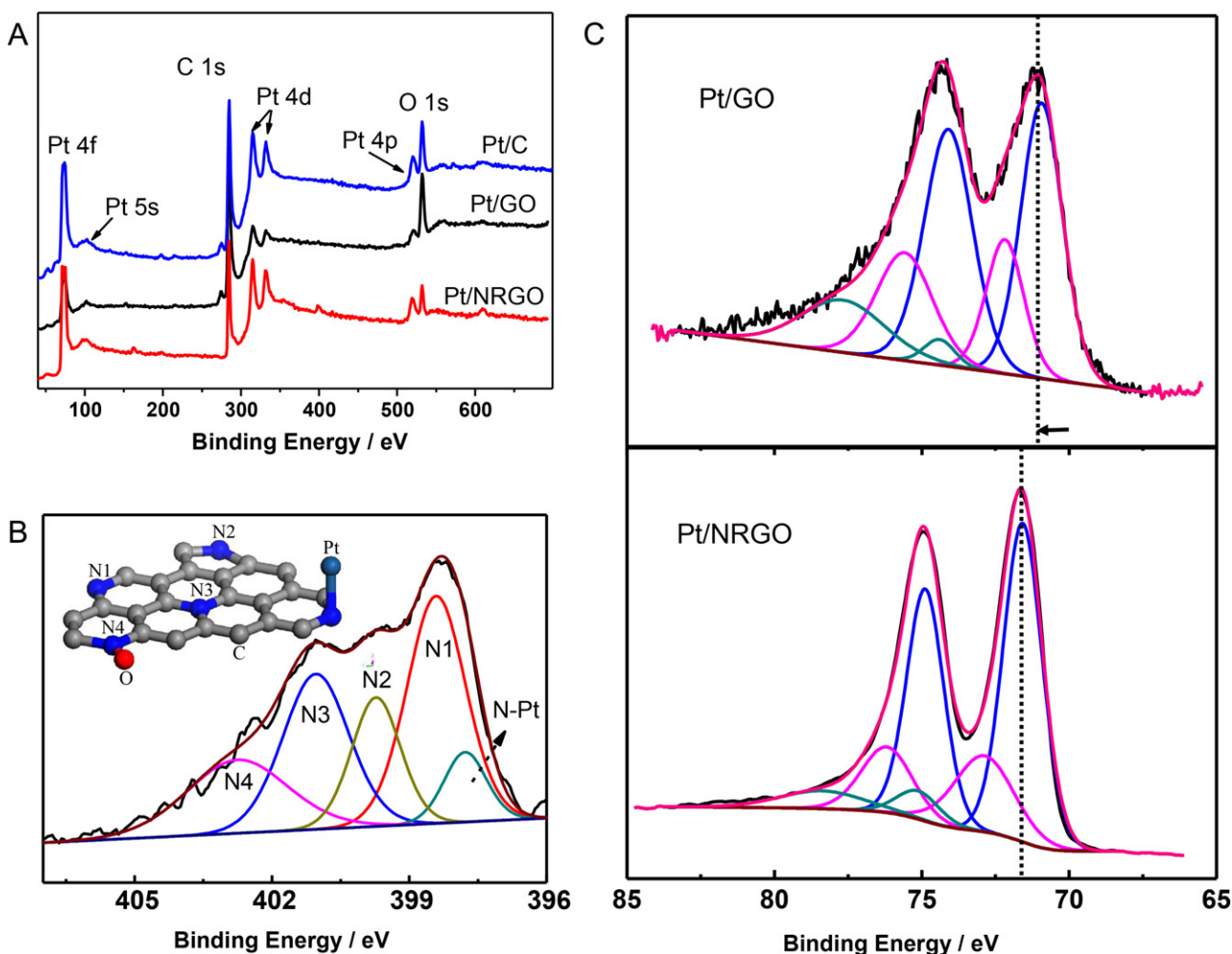


**Fig. 4.** XPS spectra of the Pt/NRGO, Pt/GO and Pt/C catalysts (A), XPS spectra of the N 1s bands (B), and XPS spectra of the Pt 4f bands (C).



and N-oxides of pyridinic-N (N4, BE =  $403.5 \pm 1.5$  eV). The nitrogen functional groups are usually in the following molecular structures (chemical states): pyridinic-N refers to nitrogen atoms at the edge of graphene planes that are bonded to two carbon atoms and donate one p electron to the aromatic  $\pi$  system, pyrrolic-N refers to nitrogen atoms that are bonded to two carbon atoms, quaternary nitrogen is also called 'graphitic nitrogen' or 'substituted nitrogen' because it is incorporated into the graphene layers by replacing a carbon atom within a graphene plane and contributes two p electrons to the  $\pi$  system, and N-oxides of pyridinic-N and pyridinic-N( $\text{N}^+-\text{O}^-$ ) are bonded to two carbon atoms and one oxygen atom [43–45]. As shown in the XPS N 1s spectrum of the Pt/NRGO (Fig. 4B), all four types of nitrogen can be observed in addition to a fifth component in the N 1s peak at a low binding energy of 398.1 eV [46,47]. This component can be assigned to a nitride, therefore indicating the presence of a metal-nitrogen bond. The different N species are formed in varying amounts and are listed in order from the most prevalent to the least prevalent: pyridinic-N and N–Pt (45.6%) > quaternary-N (25.2%) > pyrrolic-N (15.8%) > oxidized-N (13.4%). It is noted that the particular nitrogen species responsible for the interaction with platinum might be the pyridinic species, which is present in the largest amount in the NRGO. It has been demonstrated by theoretical calculations that an increased amount of nitrogen in carbon nanomaterials and the formation of pyridinic-N sites can enhance the adhesion between platinum NPs and supports and stabilise platinum in a more dispersed state [46,48].

The Pt 4f line in Fig. 4C was obtained from the Pt/NRGO and Pt/GO. The principle peaks are attributed to  $\text{Pt}^0$  at 71.4 eV (4f7/2) and 74.7 eV (4f5/2), while the peaks at 72.8 and 76.1 eV and 75.0 and 78.2 eV are assigned to Pt in the  $2^+$  and  $4^+$  states [49], respectively. The results of different Pt species are calculated based on above data and listed in Table S1. The two catalysts show essentially identical ratios of metallic Pt to oxidised species, and no significant differences are observed in the abundance ratios. However, a shift to higher energy is observed in the binding energies of the Pt/NRGO catalyst. It is known that when finely dispersed metal particles are deposited on a support, there is always a slight shift in the binding energy due to extra atomic relaxation effects [50,51]. In our case, the supported nanosized platinum particles have less pronounced bulk properties and thus are affected by the carbon support through their interactions with it. Therefore, the slight shift in the Pt peak towards higher binding energies is likely due to the presence of N sites and the effect of small particles in the Pt/NRGO catalyst.

Fig. 5A presents the curves of the Pt/NRGO, Pt/GO and Pt/C catalysts recorded at room temperature. Two peak couples are present in the CV curves of the different catalysts. One peak couple at 0.04–0.3 V is attributed to the adsorption and desorption of hydrogen on the Pt metal, and the other peak couple at 0.5–1.2 V is assumed to be due to the oxidation and reduction of the Pt metal. The ECA values were calculated by measuring the charge collected in the hydrogen adsorption–desorption region, applying a double-layer correction and assuming a value of  $210 \mu\text{C cm}^{-2}$  for the adsorption of a hydrogen monolayer [32,33]. Significantly, the Pt/NRGO gives a higher ECA value ( $75.6 \text{ m}^2 \text{ g}^{-1}$ ) than both the Pt/GO ( $64.8 \text{ m}^2 \text{ g}^{-1}$ ) and Pt/C ( $53.3 \text{ m}^2 \text{ g}^{-1}$ ) catalysts. The ECA value of the Pt/NRGO increases by 15% and 44% compared to those of the Pt/GO and Pt/C, respectively. The increase in ECA should derive from the optimized dispersion and size distribution of the Pt NPs as well as the increased conductivity of NRGO.

Polarization curves for ORR on these catalysts are shown in Fig. 5B. It can be seen that the Pt/NRGO catalyst has a higher half-wave potential by 41 and 61 mV than those of the Pt/GO and Pt/C catalysts, respectively. The diffusion-limiting currents were obtained in the potential region below 0.6 V, whereas a

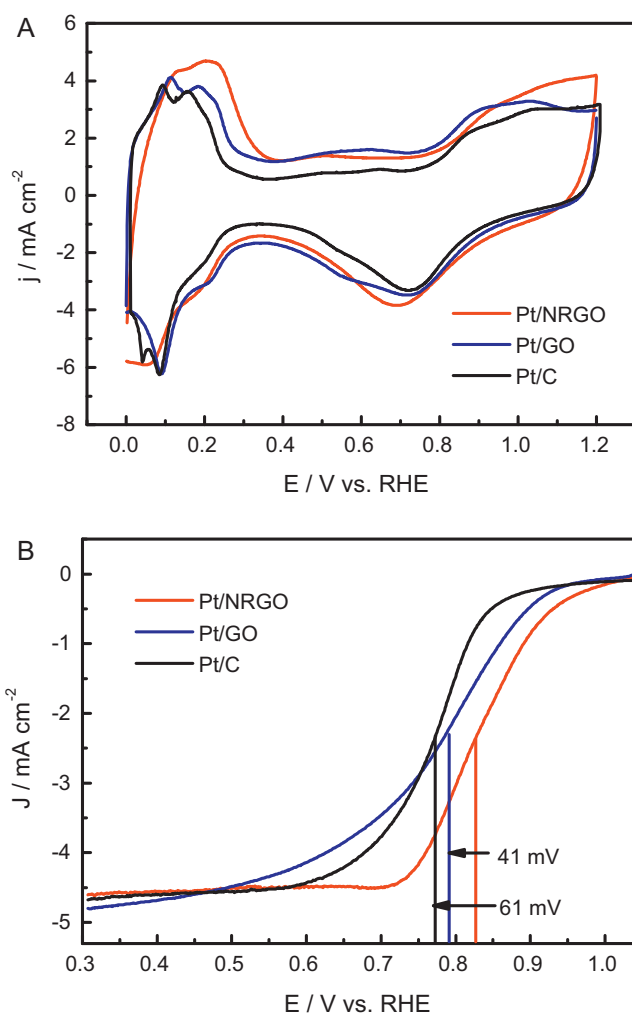


Fig. 5. CV curves of (a) and current–potential curves for ORR on (b) the Pt/NRGO, Pt/GO, and Pt/C catalysts.

mixed kinetic-diffusion control region occurs between 0.7 and 0.9 V. The kinetic current was calculated from the ORR polarization curve according to the Koutecky–Levich equation [33], which follows:

$$\frac{1}{i} = \frac{1}{i_k} + \frac{1}{i_d} \quad (4)$$

where  $i$  is the experimentally measured current,  $i_d$  is the diffusion-limiting current, and  $i_k$  is the kinetic current. Then, the kinetic current was calculated based on the following equation:

$$i_k = \frac{i \times i_d}{i_d - i} \quad (5)$$

$$\text{mass activity} = \frac{i_k}{m} \quad (6)$$

where  $m$  is the amount of Pt loading. It is believed that the diffusion-limiting currents are strongly affected by the structure of the catalyst support material. The ORR activities were calculated at 0.9 V vs. RHE. The Pt mass activity of the Pt/NRGO ( $28 \text{ A g}^{-1}$ ) is 1.3 times that of the Pt/GO ( $22 \text{ A g}^{-1}$ ) and 1.8 times that of the Pt/C ( $16 \text{ A g}^{-1}$ ), indicating that the Pt/NRGO catalyst has a higher ORR activity compared to both Pt/GO and conventional Pt/C.

The stabilities of catalysts over different electrochemical oxidation cycles are shown in Fig. 6. During voltammetric cycling between 0.6 and 1.2 V in  $\text{O}_2$ -saturated sulphuric acid, which

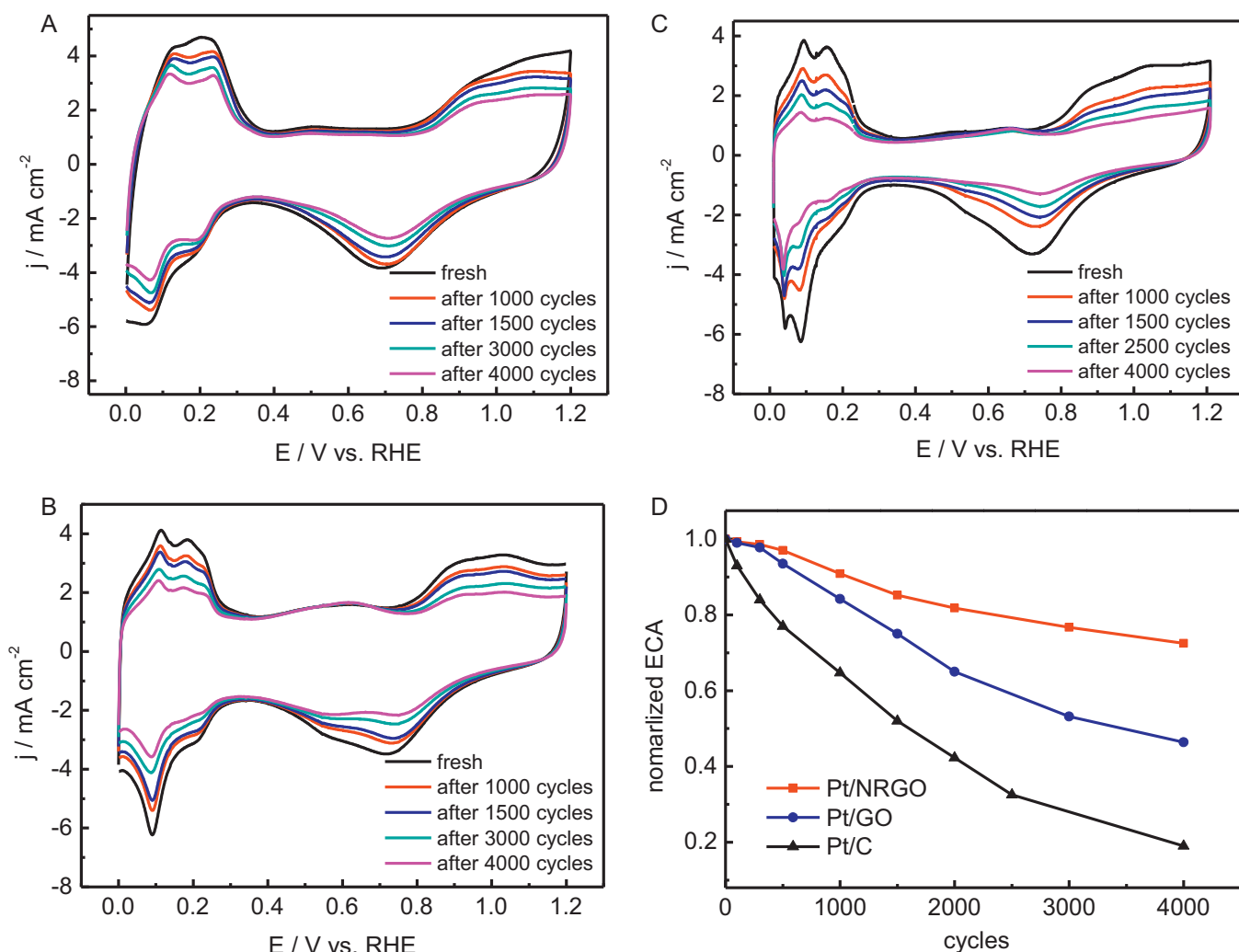
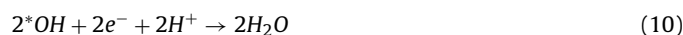


**Fig. 6.** CV curves of the Pt/NRGO (a), Pt/GO (b) and Pt/C catalysts (c) by ADT, and changes in ECA (d) of the catalysts as a function of the number of potential cycles in 0.5 mol L<sup>-1</sup> H<sub>2</sub>SO<sub>4</sub> at room temperature.

mimics the cathode of PEM fuel cells, the continuous oxidation and reduction cycling of Pt accelerates the dissolution and agglomeration of Pt. Fig. 6A–C presents the changes in the voltammograms during ADT at different intervals. Normalized by the initial voltammograms shown in Fig. 6A–C, the degradation in ECA is plotted in Fig. 6D. The ECA loss of all catalysts decreases with the number of cycles under the same ADT conditions. According to the correlations, the stability of the Pt/C catalyst is much lower than that of the Pt/GO catalyst in this work. After 4000 cycles, only 19.2% of the initial ECA of the Pt/C remains, while 31.2% of the initial ECA remains for the Pt/GO. Surprisingly, the Pt/NRGO catalyst retains 70.6% of its initial ECA after the same number of cycles. It is evident that the Pt/NRGO has a higher stability than both Pt/GO and Pt/C. These findings visibly demonstrate that under the same ADT conditions, our prepared Pt/NRGO catalyst has an electrochemical durability up to 3.7 and 2.3 times higher than those of the Pt/C and plain Pt/GO catalysts, respectively.

The ORR curves for all catalysts after 1000 cycles were also measured in the O<sub>2</sub>-saturated H<sub>2</sub>SO<sub>4</sub> electrolyte to evaluate the stability of the catalysts. As shown in Fig. 7, the Pt/C catalyst has a remarkable 86 mV degradation in the half-wave potential after ADT, while the corresponding shift for the Pt/GO catalyst is 45 mV. This degradation of the catalysts is due to the dissolution and aggregation of Pt metal in both Pt/C and Pt/GO. However, we surprisingly

found that the activity of the Pt/NRGO shows nearly no degradation relative to that of the fresh Pt/NRGO catalyst after 1000 potential cycles. Fig. 8 shows the ORR activity after 1000 cycle degradation for the Pt/NRGO, Pt/GO and Pt/C, compared with initial values (Figure 5B). The ORR performance of the Pt/C and Pt/GO decreases to 6.4 A g<sup>-1</sup> and 14.2 A g<sup>-1</sup> after 1000 cycle degradation, i.e. 64.5% and 40% of the initial ORR value. However, the activity of the Pt/NRGO after 1000 potential cycles shows nearly the same as that of the fresh Pt/NRGO. A probable reason is because the doped N can effectively stabilise the Pt NPs on NRGO as described previously. Moreover, the N-doping introduces asymmetric spin density and atomic charge density, making it possible for N-graphene to have higher electrocatalytic activities for ORR. Zhang and Xia [52] have used density functional theory to study the mechanism of ORR on the N-graphene cathode of fuel cells in an acidic environment and have shown that ORR is a four-electron pathway on N-graphene as illustrated in the following mechanism:



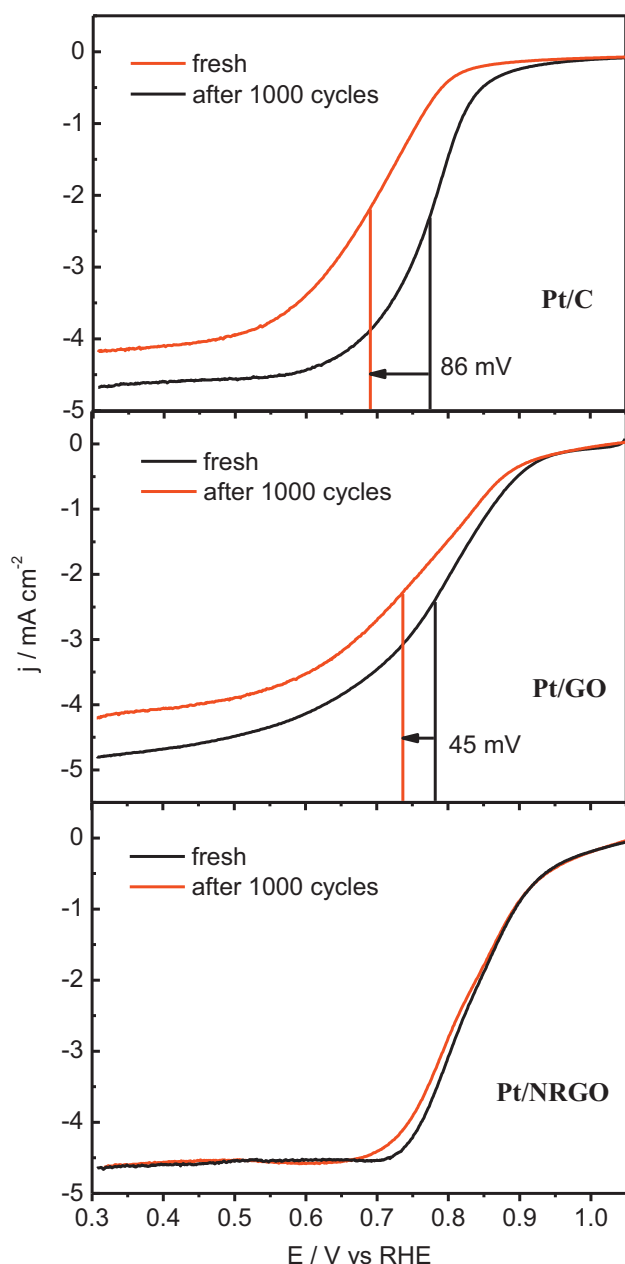


Fig. 7. Changes in the ORR activity of the catalysts after 1000 cv cycles.

where \* represents the graphene. The result is consistent with the experimental results, and the pure graphene does not exhibit this catalytic activity [20,52]. The mechanism on the Pt/NRGO with enhanced stability could be explained as shown in Scheme 2. As described earlier, the pyridinic-N is presented in the highest fraction of all the N types. It is evident that the pyridinic-N can coordinate to metal atoms (Scheme 2A). Moreover, N-containing nanostructured carbon samples with pyridinic-N as the dominant dopant will be more active for ORR. Although the dissolution and very slight aggregation of Pt metal happened on NRGO, the doped N would be exposed and act as a secondary active site to continue the ORR reaction (Scheme 2B). From the above ECA and ORR results, we can conclude that the Pt/NRGO catalyst has an excellent stability in comparison to those of the Pt/GO and conventional Pt/C catalysts.

To investigate the changes in the Pt NPs before and after ADT, the TEM images and the associated particle size distribution

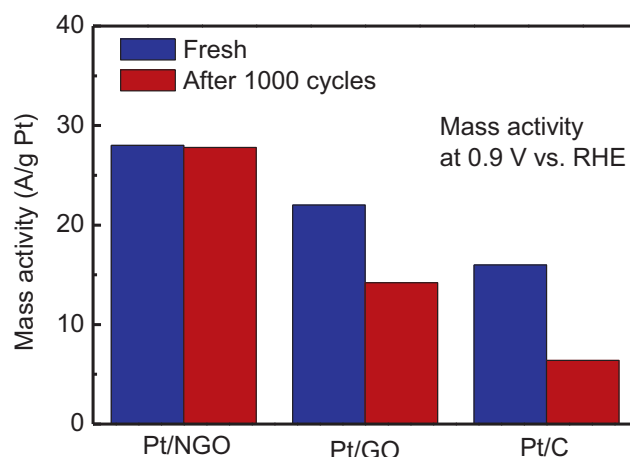
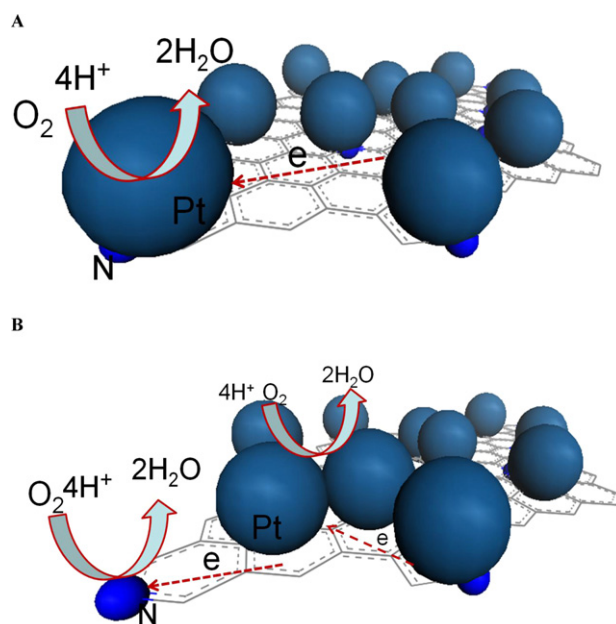


Fig. 8. Pt mass activities of the Pt/NRGO, Pt/GO and Pt/C catalysts for the ORR before and after 1000 potential cycles.

histograms after ADT are present in Fig. 9. The particle size of the Pt NPs on all three catalysts increases after 4000 CV cycles, indicating some degree of agglomeration and sintering of the Pt NPs. A comparison of the particle sizes suggests that the Pt NPs on NRGO are much smaller than those on both the Pt/GO and Pt/C samples after 4000 CV cycles. As displayed in Table 1, the average Pt particle size increases to 4.8 nm on the Pt/NRGO, and more than 55% of the particles remain under 5 nm (Fig. 9A). Interestingly, the Pt NPs smaller than 2 nm can also be observed on NRGO to a certain extent after 4000 CV cycles as shown in the high-resolution TEM images (Fig. 9B). By contrast, the average Pt particle size on the Pt/GO (Fig. 9C) increases to 8.9 nm, and more than 35% of the particles are over 10 nm. On the Pt/C, hardly any Pt metal particles are evident in the TEM images. Moreover, aggregated Pt NPs larger than 15 nm can also be observed on the Pt/C after 4000 CV cycles, indicating severe dissolution and aggregation of the Pt NPs on Pt/C (Fig. 9D).



Scheme 2. Schematic of the ORR activity for Pt/NRGO (a) before and (b) after the CV cycles.



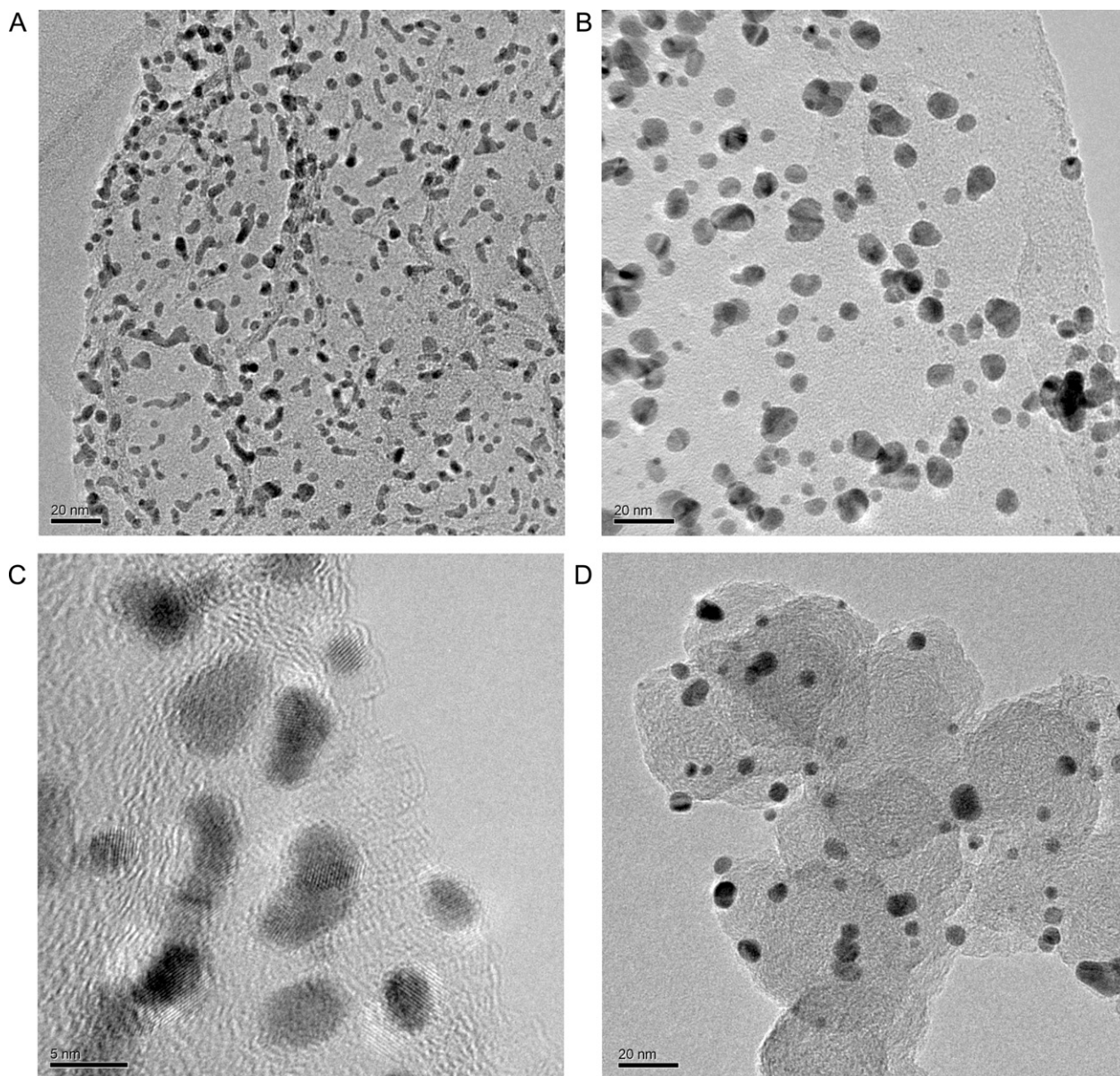


**Fig. 9.** TEM images of (a) the Pt/NRGO, (b) Pt/GO and (c) Pt/C after 4000 CV cycles.

#### 4. Conclusions

The results demonstrated experimentally for the first time the advanced nature of N-doped RGO (NRGO) prepared by a lyophilisation-assisted and mild N-doping method as a catalyst support for noble metal nanoparticles towards the ORR in PEM fuel cells. Well-dispersed Pt NPs with small particle sizes were obtained on NRGO sheets. The electrochemical tests showed that the Pt NPs supported on NRGO had higher activity and much better stability in both electrochemical surface area and oxygen reduction activity when compared to the Pt/GO and conventional Pt/C catalysts. The improved activity and stability has been attributed to (1) the optimized dispersion and size distribution of Pt NPs on NRGO, (2) the increased electrical conductivity produced by nitrogen doping, and (3) the doped N, acted as a secondary catalyst in ORR when dissolution and aggregation of Pt metal happened on NRGO. This research raises the tantalising possibility of using NRGO as a cathode catalyst support in PEM fuel cells.

#### Acknowledgments

This work was supported by the National Natural Science Foundation of China (NSFC) (50972112) and the Major State Basic Research Development Program of China (973 Program) (No.2012CB215504) and Self-determined and Innovative Research Funds of WUT (2012-ZY-008).

#### Appendix A. Supplementary data

Supplementary data associated with this article can be found, in the online version, at <http://dx.doi.org/10.1016/j.apcatb.2012.12.005>.

#### References

- [1] R.H. Baughman, A.A. Zakhidov, W.A. de Heer, *Science* 297 (2002) 787–792.
- [2] E. Antolini, *Applied Catalysis B* 88 (2009) 1–24.

- [3] S.K. Natarajan, D. Cossement, J. Hamelin, *Journal of the Electrochemical Society* 154 (2007) B310–B315.
- [4] D.P. He, K. Cheng, H.G. Li, T. Peng, F. Xu, S.C. Mu, M. Pan, *Langmuir* 28 (2012) 3979–3986.
- [5] K.S. Novoselov, A.K. Geim, S.V. Morozov, D. Jiang, M.I. Katsnelson, I.V. Grigorieva, S.V. Dubonos, A.A. Firsov, *Nature* 438 (2005) 197–200.
- [6] N. Savage, *Nature* 483 (2012) S30–S31.
- [7] G. Eda, G. Fanchini, M. Chhowalla, *Nature Nanotechnology* 3 (2008) 270–274.
- [8] Y. Zheng, J. Liu, J. Liang, M. Jaroniec, S.Z. Qiao, *Energy & Environmental Science* 5 (2012) 6717–6731.
- [9] R.I. Jafri, N. Rajalakshmi, S. Ramaprabhu, *Journal of Materials Chemistry* 20 (2010) 7114–7117.
- [10] X. Li, H. Wang, J.T. Robinson, H. Sanchez, G. Diankov, H. Dai, *Journal of the American Chemical Society* 131 (2009) 15939–15944.
- [11] V. Di Noto, E. Negro, *Electrochimica Acta* 55 (2010) 7564–7574.
- [12] V. Di Noto, E. Negro, S. Polizzi, P. Riello, P. Atanassov, *Applied Catalysis B* 111 (2012) 185–199.
- [13] V. Di Noto, E. Negro, R. Gliubbizzi, S. Lavina, G. Pace, S. Gross, C. Maccato, *Advanced Functional Materials* 17 (2007) 3626–3638.
- [14] V. Di Noto, E. Negro, K. Vezzù, L. Toniolo, G. Pace, *Electrochimica Acta* 57 (2011) 257–269.
- [15] Y. Wang, Y. Shao, D.W. Matson, J. Li, Y. Lin, *ACS Nano* 4 (2010) 1790–1798.
- [16] X. Wang, X. Li, L. Zhang, Y. Yoon, P.K. Weber, H. Wang, J. Guo, H. Dai, *Science* 324 (2009) 768–771.
- [17] F. Cervantes-Sodi, G. Csanyi, S. Pisanec, A.C. Ferrari, *Physical Review B* 77 (2008) 165427–165430.
- [18] Y.Y. Shao, J.H. Sui, G.P. Yin, Y.Z. Gao, *Applied Catalysis B* 79 (2008) 89–99.
- [19] C.W. Zhou, J. Kong, E. Yenilmez, H.J. Dai, *Science* 290 (2000) 1552–1555.
- [20] L.T. Qu, Y. Liu, J.B. Baek, L.M. Dai, *ACS Nano* 4 (2010) 1321–1326.
- [21] F. Jaouen, E. Proietti, M. Lefevre, R. Chenitz, J.P. Dodelet, G. Wu, H.T. Chung, C.M. Johnston, P. Zelenay, *Energy & Environmental Science* 4 (2011) 114–130.
- [22] M. Lefevre, E. Proietti, F. Jaouen, J.P. Dodelet, *Science* 324 (2009) 71–74.
- [23] H. Meng, N. Larouche, M. Lefevre, F. Jaouen, B. Stansfield, J.P. Dodelet, *Electrochimica Acta* 55 (2010) 6450–6461.
- [24] A. Gomathi, S. Reshma, C.N.R. Rao, *Journal of Solid State Chemistry* 182 (2009) 72–76.
- [25] D.R. Dreyer, S. Park, C.W. Bielawski, R.S. Ruoff, *Chemical Society Reviews* 39 (2010) 228–240.
- [26] Z.Y. Lin, G. Waller, Y. Liu, M.L. Liu, C.P., Wong, *Advanced Energy Materials* doi: 10.1002/aenm.201200038.
- [27] D.P. He, S.C. Mu, M. Pan, *International Journal of Hydrogen Energy* 37 (2012) 4699–4703.
- [28] Z. Wei, D. Wang, S. Kim, S.Y. Kim, Y. Hu, M.K. Yakes, A.R. Laracuente, Z. Dai, S.R. Marder, C. Berger, W.P. King, W.A. de Heer, P.E. Sheehan, E. Riedo, *Science* 328 (2010) 1373–1376.
- [29] W.S. Hummers, R.E. Offeman, *Journal of the American Chemical Society* 80 (1958), 1339–1339.
- [30] C. Bock, C. Paquet, M. Couillard, G.A. Botton, B.R. MacDougall, *Journal of the American Chemical Society* 126 (2004) 8028–8037.
- [31] V. Radmilovic, H.A. Gasteiger, P.N. Ross, *Journal of Catalysis* 154 (1995) 98–106.
- [32] T.J. Schmidt, H.A. Gasteiger, G.D. Stab, P.M. Urban, D.M. Kolb, R.J. Behm, *Journal of the Electrochemical Society* 145 (1998) 2354–2358.
- [33] B. Lim, M. Jiang, P.H.C. Camargo, E.C. Cho, J. Tao, X. Lu, Y. Zhu, Y. Xia, *Science* 324 (2009) 1302–1305.
- [34] S.B. Yin, S.C. Mu, H.F. Lv, N.C. Cheng, M. Pan, Z.Y. Fu, *Applied Catalysis B* 93 (2010) 233–240.
- [35] M. Sprinkle, D. Siegel, Y. Hu, J. Hicks, A. Tejada, A. Taleb-Ibrahimi, P. Le Fevre, F. Bertran, S. Vizzini, H. Enriquez, S. Chiang, P. Soukiasian, C. Berger, W.A. de Heer, A. Lanzara, E.H. Conrad, *Physical Review Letters* 103 (2009) 226803–226806.
- [36] C. Thomsen, S. Reich, *Physical Review Letters* 85 (2000) 5214–5217.
- [37] D. Wei, Y. Liu, Y. Wang, H. Zhang, L. Huang, G. Yu, *Nano Letters* 9 (2009) 1752–1758.
- [38] L.S. Panchokarla, K.S. Subrahmanyam, S.K. Saha, A. Govindaraj, H.R. Krishnamurthy, U.V. Waghmare, C.N.R. Rao, *Advanced Materials* 21 (2009) 4726–4730.
- [39] M.D. Stoller, S. Park, Y. Zhu, J. An, R.S. Ruoff, *Nano Letters* 8 (2008) 3498–3502, 8.
- [40] D.P. He, K. Cheng, T. Peng, X.L. Sun, M. Pan, S.C. Mu, *Journal of Materials Chemistry* 22 (2012) 21298–21304.
- [41] Y. Wang, S.Q. Song, V. Maragou, P.K. Shen, P. Tsiakaras, *Applied Catalysis B* 89 (2009) 223–228.
- [42] Y.L. Hsin, K.C. Hwang, C.T. Yeh, *Journal of the American Chemical Society* 129 (2007) 9999–10010.
- [43] P.H. Matter, L. Zhang, U.S. Ozkan, *Journal of Catalysis* 239 (2006) 83–96.
- [44] S. Kundu, T.C. Nagaiah, W. Xia, Y. Wang, S.V. Dommele, J.H. Bitter, M. Santa, G. Grundmeier, M. Bron, W. Schuhmann, M. Muhler, *Journal of Physical Chemistry C* 113 (2009) 14302–14310.
- [45] R. Arrigo, M. Havecker, R. Schlögl, D.S. Su, *Chemical Communications* 40 (2008) 4891–4893.
- [46] P.L. Kuo, W.F. Chen, H.Y. Huang, I.C. Chang, S.A. Dai, *Journal of Physical Chemistry B* 110 (2006) 3071–3077.
- [47] A. Adenier, M.M. Chehimi, I. Gallardo, J. Pinson, N. Vila, *Langmuir* 20 (2004) 8243–8253.
- [48] G. Wu, D. Li, C. Dai, D. Wang, N. Li, *Langmuir* 24 (2008) 3566–3575.
- [49] P. Bera, K.R. Priolkar, A. Gayen, P.R. Sarode, M.S. Hegde, S. Emura, R. Kumashiro, V. Jayaram, G.N. Subbanna, *Chemistry of Materials* 15 (2003) 2049–2060.
- [50] G.K. Wertheim, S.B. Diczko, *Physical Review B* 37 (1988) 844–847.
- [51] A. Bourane, D. Bianchi, *Journal of Catalysis* 222 (2004) 499–510.
- [52] L. Zhang, Z. Xia, *Journal of Physical Chemistry C* 115 (2011) 11170–11176.